

*ARMY RESEARCH LABORATORY*



## **Multispecies Reacting Flow Model for the Plasma Efflux of an ETC Igniter-Application to an Open-Air Plasma Jet Impinging on an Instrumented Plate**

**by Michael J. Nusca, William R. Anderson, and Michael J. McQuaid**

**ARL-TR-3275**

**August 2004**

## **NOTICES**

### **Disclaimers**

The findings in this report are not to be construed as an official Department of the Army position unless so designated by other authorized documents.

Citation of manufacturer's or trade names does not constitute an official endorsement or approval of the use thereof.

Destroy this report when it is no longer needed. Do not return it to the originator.

# **Army Research Laboratory**

Aberdeen Proving Ground, MD 21005-5066

---

**ARL-TR-3275**

**August 2004**

---

## **Multispecies Reacting Flow Model for the Plasma Efflux of an ETC Igniter-Application to an Open-Air Plasma Jet Impinging on an Instrumented Plate**

**Michael J. Nusca, William R. Anderson, and Michael J. McQuaid**  
**Weapons and Materials Research Directorate, ARL**

<b>REPORT DOCUMENTATION PAGE</b>				<i>Form Approved OMB No. 0704-0188</i>
Public reporting burden for this collection of information is estimated to average 1 hour per response, including the time for reviewing instructions, searching existing data sources, gathering and maintaining the data needed, and completing and reviewing the collection information. Send comments regarding this burden estimate or any other aspect of this collection of information, including suggestions for reducing the burden, to Department of Defense, Washington Headquarters Services, Directorate for Information Operations and Reports (0704-0188), 1215 Jefferson Davis Highway, Suite 1204, Arlington, VA 22202-4302. Respondents should be aware that notwithstanding any other provision of law, no person shall be subject to any penalty for failing to comply with a collection of information if it does not display a currently valid OMB control number.				
<b>PLEASE DO NOT RETURN YOUR FORM TO THE ABOVE ADDRESS.</b>				
1. REPORT DATE (DD-MM-YYYY)	2. REPORT TYPE			3. DATES COVERED (From - To)
August 2004	Final			January 2000–December 2002
4. TITLE AND SUBTITLE				5a. CONTRACT NUMBER
Multispecies Reacting Flow Model for the Plasma Efflux of an ETC Igniter-Application to an Open-Air Plasma Jet Impinging on an Instrumented Plate				5b. GRANT NUMBER
				5c. PROGRAM ELEMENT NUMBER
				5d. PROJECT NUMBER
				622618H8000
				5e. TASK NUMBER
				5f. WORK UNIT NUMBER
7. PERFORMING ORGANIZATION NAME(S) AND ADDRESS(ES)				8. PERFORMING ORGANIZATION REPORT NUMBER
U.S. Army Research Laboratory ATTN: AMSRD-ARL-WM-BD Aberdeen Proving Ground, MD 21005-5066				ARL-TR-3275
9. SPONSORING/MONITORING AGENCY NAME(S) AND ADDRESS(ES)				10. SPONSOR/MONITOR'S ACRONYM(S)
				11. SPONSOR/MONITOR'S REPORT NUMBER(S)
12. DISTRIBUTION/AVAILABILITY STATEMENT				
Approved for public release; distribution is unlimited.				
13. SUPPLEMENTARY NOTES				
14. ABSTRACT				
The U.S. Army Research Laboratory (ARL) is investigating the electrothermal-chemical (ETC) gun concept. As part of this program, ARL has undertaken a comprehensive study on the interaction of the plasma efflux from an ETC igniter with solid propellant grains. The goal of this work is to elucidate the physical, mechanical, and chemical mechanisms that underlie the observed ballistic effects in ETC guns that lead to performance gains. This report describes the first phase of the modeling effort in support of this plasma-propellant interaction project. A time-accurate computational fluid dynamics code is used that includes high-temperature thermodynamics, variable specific heats and transport properties (viscosity and thermal conductivity), and finite-rate (nonequilibrium) chemical kinetics. Validation of this code uses a series of experiments with an ETC igniter fired into open air, generating an unsteady flowfield in which an instrumented plate is placed. Computer simulations reveal important gas dynamic and chemical details of the plasma jet as the jet mixes with air and interacts with the plate, representing a unique model of the ETC plasmas.				
15. SUBJECT TERMS				
gun charges, solid propellant, multiphase flow, computer simulation				
16. SECURITY CLASSIFICATION OF:		17. LIMITATION OF ABSTRACT	18. NUMBER OF PAGES	19a. NAME OF RESPONSIBLE PERSON Michael J. Nusca
a. REPORT UNCLASSIFIED	b. ABSTRACT UNCLASSIFIED	c. THIS PAGE UNCLASSIFIED	UL 36	19b. TELEPHONE NUMBER (Include area code) (410) 278-6108

---

## **Contents**

---

<b>List of Figures</b>	<b>iv</b>
<b>List of Tables</b>	<b>v</b>
<b>Acknowledgments</b>	<b>vi</b>
<b>1. Introduction</b>	<b>1</b>
<b>2. Experimental Efforts for PPI</b>	<b>2</b>
<b>3. Previous Modeling Efforts</b>	<b>4</b>
<b>4. Multispecies Reacting Flow CFD Code</b>	<b>4</b>
<b>5. Results and Discussion</b>	<b>12</b>
<b>6. Conclusions</b>	<b>22</b>
<b>7. References</b>	<b>23</b>
<b>Distribution List</b>	<b>26</b>

---

## List of Figures

---

Figure 1. ETC gun concept .....	1
Figure 2. Schematic of ARL open-air experiment (also showing computational domain). .....	3
Figure 3. Schematic of the PSU experimental setup.....	3
Figure 4. Measured/computed pressure at the probe tip .....	5
Figure 5. Computed pressure contours at probe .....	5
Figure 6. Computational grid used for the simulation of the Penn State University open-air plate experiment. Lower boundary corresponds to the capillary and plate centerline. Partial grid shown for clarity. ....	13
Figure 7. Current history.....	13
Figure 8. Efflux density and velocity histories .....	14
Figure 9. Efflux pressure and temperature histories .....	14
Figure 10. Efflux species mole fraction histories. ....	15
Figure 11. Schematic of gasdynamic features in a highly underexpanded jet.....	15
Figure 12. Computed (a) Mach number contours and (b) temperature contours at time = 0.0208 ms.....	16
Figure 13. Computed (a) Mach number contours and (b) temperature contours at time = 0.0458 ms.....	16
Figure 14. Computed (a) Mach number contours and (b) temperature contours at time = 0.0708 ms.....	17
Figure 15. Computed (a) Mach number contours and (b) temperature contours at time = 0.1192 ms.....	17
Figure 16. Computed (a) Mach number contours and (b) temperature contours at time = 0.1494 ms.....	18
Figure 17. Computed (a) Mach number contours and (b) temperature contours at time = 0.1714 ms.....	18
Figure 18. Computed (a) Mach number contours and (b) temperature contours at time = 0.2410 ms.....	19
Figure 19. Computed pressures at plate taps. ....	19
Figure 20. Peak pressure data and computations.....	20
Figure 21. Computed and measured pressure histories at (a) P4 and (b) P1 tap locations.....	20
Figure 22. Computed time variation of mole fractions at two locations on the plate.....	21
Figure 23. Computed mole fraction contours for (a) O <sub>2</sub> and (b) C at time = 0.0262 ms. ....	21
Figure 24. Computed mole fraction contours for CO at times = (a) 0.0262 and (b) 0.0458 ms. ....	22

---

## **List of Tables**

---

Table 1. Chemical kinetics mechanism ( <i>10</i> ).....	10
Table 2. Rate data for special reactions. ....	11
Table 3. Reaction rate efficiencies.....	11

---

## Acknowledgments

---

The Plasma-Propellant Interaction Workunit, headed by Dr. Richard Beyer at the U.S. Army Research Laboratory (ARL), funded this project. The Department of Defense Major Shared Resources Centers supplied supercomputer time at ARL and the Naval Oceanographic Office.

---

## 1. Introduction

---

Future military engagements will require weapons systems exhibiting improved range and accuracy. One of the technologies under investigation to achieve these goals is the electrothermal-chemical (ETC) propulsion concept shown schematically in figure 1. In the ETC gun, energy that is stored either in batteries or in a rotating device is converted on demand into an electrically generated plasma (resulting from the ablation of polyethylene material in a capillary) that is injected into the chamber in a howitzer or gun. This plasma energy is used to ignite the chemical propulsion charge (i.e., solid propellant) as well as enhance gun performance by taking advantage of a number of unique plasma characteristics. For example, a low-density plasma jet can efficiently ignite charges of high-loading density, can control propellant mass generation rates (1), can reduce propellant charge temperature sensitivity (i.e., the variation of gun performance with changing ambient temperature (2, 3) and can shorten ignition delay (i.e., the time interval between firing of the igniter and ignition of the propellant (4). Plasma igniters eliminate the conventional chemical igniter and thus can enhance the safety aspects of the overall gun propulsion system.

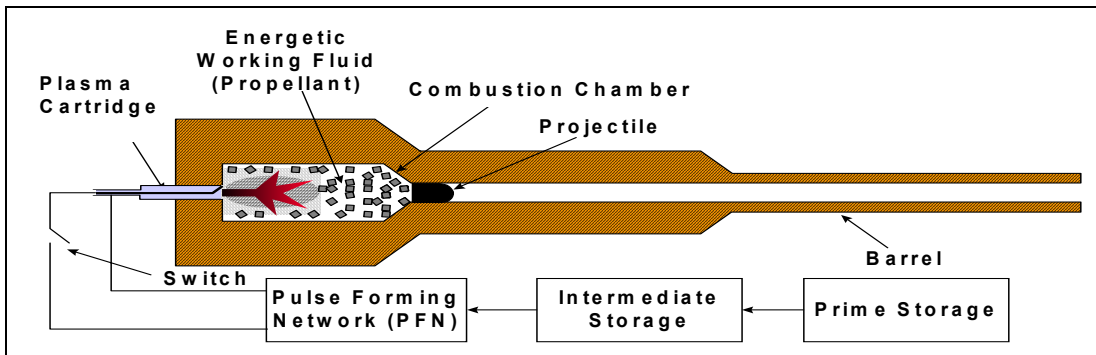


Figure 1. ETC gun concept.

Research has been carried out on many aspects of plasmas related to uses such as solid propellant igniters (5, 6). Because the plasma is at a temperature (typically  $>10,000$  K) that is considerably higher than conventional chemical igniters (3000 K), the radiation properties of the plasma have also been considered. The high plasma temperature leads to radiation effects nearly 100 times greater than that of chemical igniters (i.e., a  $T^4$  effect) (5). Such radiation could lead to significantly different temperature profiles within the propellant, causing changes in combustion rates. Plasma has a much lower density than the gases generated by a chemical igniter. This will impact the convective heat transfer to the propellant, as the plasma moves through the grains as well as the velocity and mode of flamespreading within a propellant bed. It has been suggested that energy transport by convection may be as important as radiation transport in plasma-propellant interactions (PPI) (7, 8).

All of the effects described previously can lead to significant changes in ballistic behavior and useful improvements in gun performance, but an understanding of the underlying physical mechanisms is necessary to achieve this goal. To this end, the U.S. Army Research Laboratory (ARL) has begun a comprehensive study on the interaction of the plasma efflux from an ETC igniter with solid propellant grains. The goal of this work is to elucidate the relevant physical, mechanical, and chemical mechanisms that underlie the observed ballistic effects. Various aspects of the experimental program for PPI are described elsewhere (9, 12). The first phase of the modeling effort in support of this PPI project involves a time-accurate computational fluid dynamics (CFD) code that has been written to include high-temperature thermodynamics, variable specific heats and transport properties (viscosity and thermal conductivity), and finite-rate (nonequilibrium) chemical kinetics (the mechanism is described in reference (10)). A separate capillary model described by McQuaid and Nusca (11) supplies boundary conditions for the CFD code in terms of the physical and chemical properties of the plasma capillary efflux. Validation of the capillary model and the CFD code, including coupled chemistry, is conducted by simulating a series of experiments wherein a plasma jet is generated from a plasma cartridge; pressures in the resulting unsteady flowfield are measured using probes mounted on a plate held normal to the efflux.

---

## 2. Experimental Efforts for PPI

---

White et al. (8) and Williams and White (12) documented the plasma-propellant interaction experiments conducted at ARL. The general view of the plasma generator is shown in figure 2. The plasma capillary consists of a standard polyethylene liner with dimensions 102 mm in length and 6.35 mm in diameter. The nozzle consists of a circular tube of 2.9 cm in length and 1.3 cm in diameter that is directly adjacent to the end of the plasma capillary followed by another circular tube of 1.9 cm in length and 3.2 cm in diameter. As a result, the plasma efflux generated by the capillary is expanded through a step-configuration nozzle before emerging into the open air. A pressure probe is positioned in the path of the plasma efflux (figure 2). To protect this probe, the plasma capillary is mounted behind a steel plate. The pressure probe was placed 15 cm away from the surface of the plate and aligned with the centerline of the cartridge. Care was exercised in shielding the gage from direct interaction with the plasma as were the cables and amplifiers (strong evidence of charged particle impact on the unshielded gage was found [8]). Even so, post-firing examination of the pressure gage indicated significant amounts of particulate in the plasma effluent (the plasma is generated by ablation) that contributed to noticeable variability in pressure histories from shot to shot. Currently, R. A. Beyer of ARL is conducting a new set of experiments in which the plasma efflux is injected into a closed chamber (13).

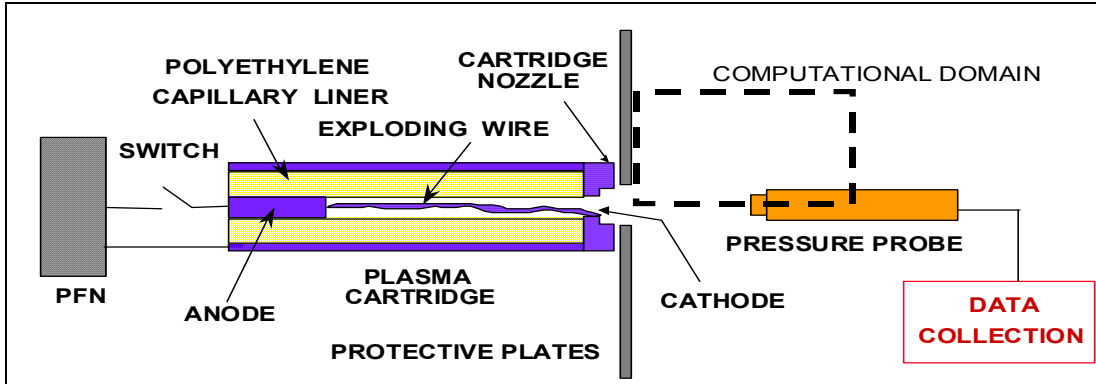


Figure 2. Schematic of ARL open-air experiment (also showing computational domain).

Litzinger et al. (14) of Penn State University (PSU) have designed and operated two PPI experiments. The open-air experiment is shown schematically in figure 3. The polyethylene capillary is typically 26 mm in length and 3 mm in diameter ( $d$ ). An extension tube 26 mm in length is placed at the capillary exit, which guides the plasma efflux into the open-air. The capillary and the extension tube are mounted within a solid housing (not shown in figure 3) making the setup similar to that shown in figure 2 (i.e., the protective plate mounted near the capillary exit). An instrumented plate is placed at some distance ( $L$ ) from the plasma device, typically 19 mm. Pressure probes are mounted on the plate with a spacing of 9.53 mm (3/8 in).

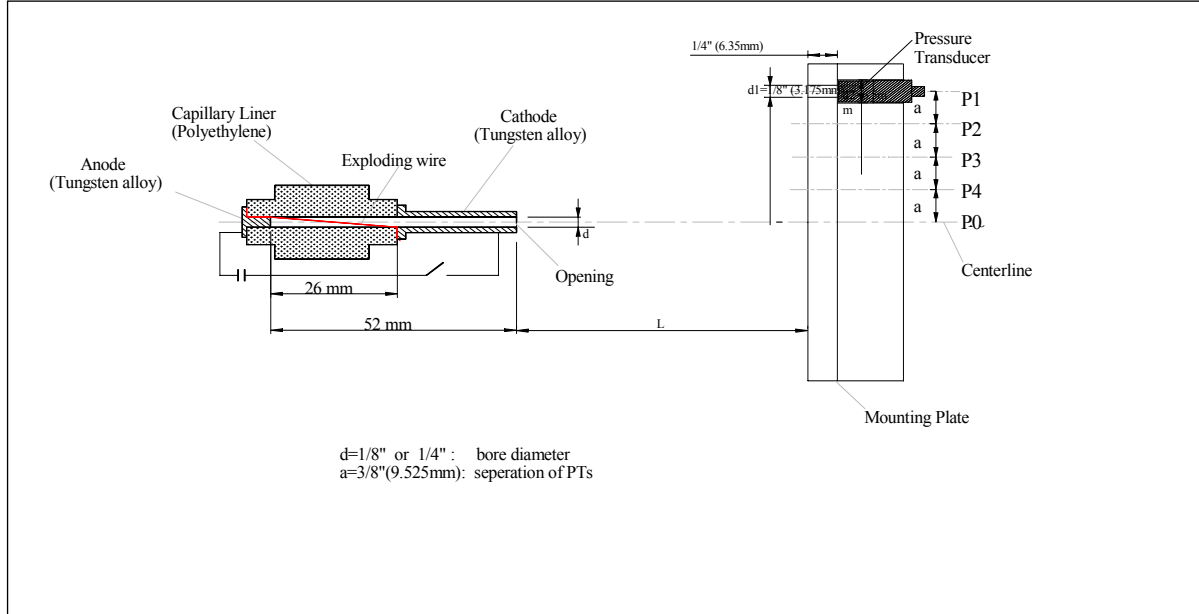


Figure 3. Schematic of the PSU experimental setup.

---

### **3. Previous Modeling Efforts**

---

The initial modeling effort for open-air plasma discharges was conducted at ARL from 1997 to 1998 (15–16). This computational study was based on the National Research Laboratory (NRL) CFD code FAST3D (17) and sponsored by the Department of Defense (DOD) Common High-Performance Computing (HPC) Software Support Initiative (CHSSI) program. The ARL open-air plasma experiment, shown schematically in figure 2, was chosen as a test case for the FAST3D CFD code because the plasma jet is of very high velocity and temperature, but very low density. The plasma jet was assumed to be an ideal, neutral, single-component gas with density, temperature, ratio of specific heats ( $\gamma$ ), and velocity characteristics identical to the plasma discharge. The multicomponent nature of the plasma, consisting of various neutral species, ions, and electrons, and its chemical reactivity were not considered in those studies. The augmentation of plasma-air mixing, caused by viscosity and turbulence, was also excluded in these studies. The time-dependent gas properties, along with jet velocity and  $\gamma$  were determined using a plasma capillary code developed at ARL by J. Powell (18). Overall, these CFD simulations captured the major features of the plasma jet as photographed by White et al. (5). Alternating bright-dark structures in the photos were identified as the shock structures in the jet. A precursor shock caused by the high-velocity/low-density plasma effluent (a feature not easily photographed) was captured. Comparisons between computed and measured pressures in the jet were encouraging but pointed to the need for a variable  $\gamma$ , multicomponent, reacting flow model.

More advanced modeling was conducted by Nusca et al. (19) in 1999–2000 and is continued in the present effort (see section 4 for a description of the model). Figures 4 and 5 show some typical results from that effort. The ARL open-air plasma jet experiment was used for code validation. Figure 4 demonstrates the model’s utility in matching the time-of-arrival of the precursor shock (shown just passing over the probe tip in figure 5) and the stagnation pressure of ~7 MPa (pressure values in figure 5 are nondimensional so that a value of 40 corresponds to a pressure of ~4 MPa). Although these comparisons are good, it was felt that a better agreement between predicted and measured pressure values was required. This report discusses a comparison between this model and the Penn State open-air/plate experiment (figure 3).

---

### **4. Multispecies Reacting Flow CFD Code**

---

The high-temperature, nonideal chemically reacting gas flowfield within the capillary efflux jet is numerically simulated using CFD. The NSRG2 code (20–22) solves the 2-D/axisymmetric, unsteady real-gas Navier-Stokes equations including submodels that represent finite-rate

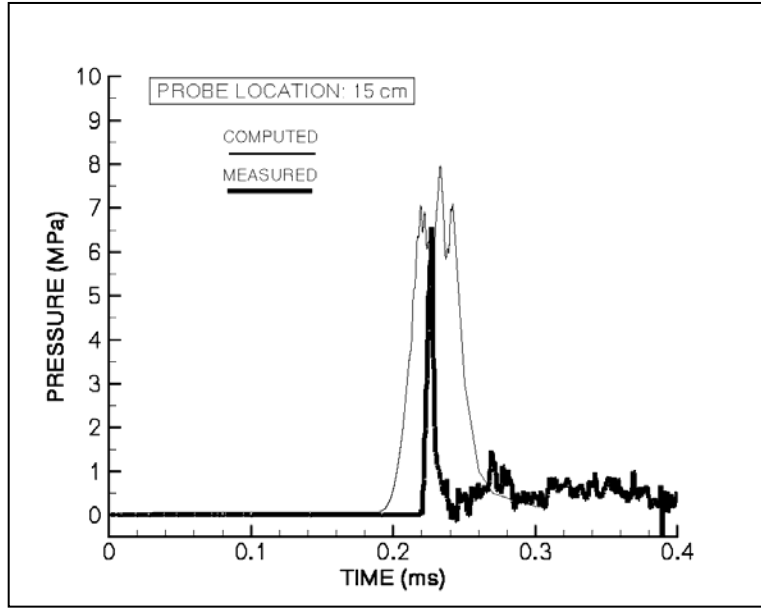


Figure 4. Measured/computed pressure at the probe tip.

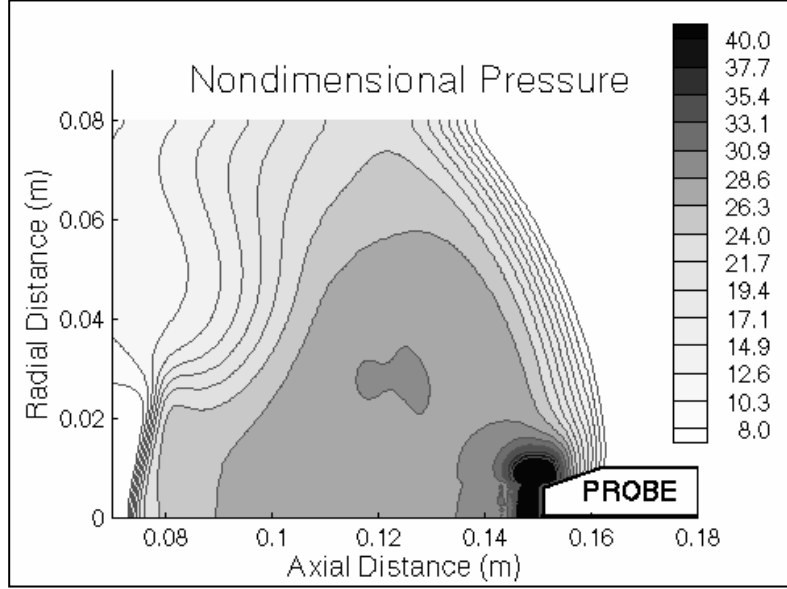


Figure 5. Computed pressure contours at probe.

(nonequilibrium) chemical reactions, multispecies diffusion, as well as variable specific heats, viscosity, and thermal conductivity. These partial differential equations are cast in conservation form and converted to algebraic equations using a finite-volume formulation. Solution takes place on a mesh of nodes distributed in a zonal fashion throughout the flowfield such that sharp geometric corners and other details are accurately represented. The conservation law form of the equations ensures that the end states of regions of discontinuity (e.g., shocks) are physically correct even when smeared over a few computational cells. The Navier-Stokes equations for

2-D/axisymmetric ( $x, y$  coordinates), reacting ( $N$  species) and unsteady (time,  $t$ ) flow are written in nondimensional form (20). The dependent variables are density ( $\rho$ ), velocity ( $V$  and components  $u, v$ ), energy ( $e$ ), and species mass fraction ( $c_i$ ). Pressure and temperature are  $p$  and  $T$ , whereas  $L$  is a characteristic lengthscale for the flowfield.

$$\frac{\partial U}{\partial t} + \frac{\partial F}{\partial x} + \frac{\partial G}{\partial y} + H = 0,$$

$$U = \left\{ \rho y^\alpha, \rho u y^\alpha, \rho v y^\alpha, \rho e y^\alpha, \rho c_1 y^\alpha, \dots, \rho c_N y^\alpha \right\},$$

$$H = \left\{ 0, 0, \alpha \sigma_+, 0, -w_1, \dots, -w_N \right\},$$

$$F = \begin{Bmatrix} \rho u y^\alpha \\ (\rho u^2 + \sigma_{xx}) y^\alpha \\ (\rho u v + \tau_{xy}) y^\alpha \\ (\rho u e + u \sigma_{xx} + v \tau_{xy} + q_x) y^\alpha \\ (\rho u c_1 - \Lambda_1(c_1)_x - \Gamma_1(\ln T)_x) y^\alpha \\ \vdots \\ \vdots \\ (\rho u c_N - \Lambda_N(c_N)_x - \Gamma_N(\ln T)_x) y^\alpha \end{Bmatrix}, \quad G = \begin{Bmatrix} \rho v y^\alpha \\ (\rho v u + \tau_{yx}) y^\alpha \\ (\rho v^2 + \sigma_{yy}) y^\alpha \\ (\rho v e + v \sigma_{yy} + u \tau_{xy} + q_y) y^\alpha \\ (\rho v c_1 - \Lambda_1(c_1)_y - \Gamma_1(\ln T)_y) y^\alpha \\ \vdots \\ \vdots \\ (\rho v c_N - \Lambda_N(c_N)_y - \Gamma_N(\ln T)_y) y^\alpha \end{Bmatrix},$$

$$\begin{aligned} \sigma_{xx} &= y^\alpha p + \frac{2\mu}{3y^\alpha Re} \left( \frac{\partial(y^\alpha u)}{\partial x} + \frac{\partial(y^\alpha v)}{\partial y} \right) - \frac{2\mu}{Re} \frac{\partial u}{\partial x}, & q_x &= \frac{-\kappa}{Re Pr E} \frac{\partial T}{\partial x} - \frac{\mu}{Re Pr} \sum_{i=1}^N Le h_i \frac{\partial c_i}{\partial x} \\ \sigma_+ &= p + \frac{2\mu}{3y^\alpha Re} \left( \frac{\partial(y^\alpha u)}{\partial x} + \frac{\partial(y^\alpha v)}{\partial y} \right) - \frac{2\mu}{Re} \frac{v}{y^\alpha}, & \tau_{xy} &= \tau_{yx} = \frac{-\mu}{y^\alpha Re} \left( \frac{\partial u}{\partial y} + \frac{\partial v}{\partial x} \right), \end{aligned} \quad (1)$$

where  $\sigma_{yy}$  and  $q_y$  are similarly written and  $E = V^2/h$ ,  $\kappa = k_T \Lambda$ ,  $\Lambda = \mu Le/RePr$ ,  $Le = Pr/Sc$ ,  $Pr = \mu c_p/\kappa$ ,  $Sc = \mu/\rho D$ , and  $Re = \rho VL/\mu$ . The Navier-Stokes equations (equation 1) are written in integral form and then re-expressed in a semi-discrete fashion using a finite-volume discretization technique. The numerical computations proceed by solving the semi-discrete equation on each computational cell using central and upwind numerical differences along with flux limiting. Once properly discretized, the resulting set of algebraic equations is solved in a coupled manner in time using an explicit time-accurate method. The numerical time-step is computed using the CFL condition. A separate chemical time-step is computed as well. The final time-step is based on the smallest of these. Nusca (20–22) provides a more complete description of the numerical scheme.

The diffusion coefficient,  $D$ , is understood to be the multicomponent coefficient,  $D_{im}$  (specie  $i$  into the mixture), which is related to the binary diffusion coefficient,  $D_{ij}$  (specie  $i$  diffusing into specie  $j$ ),

$$D_{im} = \frac{1 - X_i}{\sum_j X_j / D_{ij}} \quad ; \quad D_{ij} = \frac{0.00266 T^{3/2}}{p M_{ij}^{1/2} \sigma_{ij}^2 \Omega_D} \quad , \quad (2)$$

where  $X_i$  is the mole fraction and  $M_i$  is the molecular weight of specie  $i$ ,  $\Omega_D$  is the collision integral and  $\sigma_{ij}$  is the collision diameter (available in the literature). The thermal diffusion ratio,  $k_T$ , is assumed to be 1.0. Because no provisions have been made in the conservation equations (equation 1) for flows with electric currents at this time, the flowfield was rendered electrically neutral by setting the diffusion velocity of the electrons equal to the average diffusion velocity of the ions—the diffusion coefficient for the electrons is then computed from that of the ions. Future works will be aimed at relaxing this assumption by allowing for charge separation effects and including appropriate source terms in the momentum and energy equations.

We realize that the plasma gas does not necessarily behave as a perfect fluid. Indeed, the ionized gas is usually characterized as rarefied and one in which Coulomb interactions between charged particles create significant departures from the perfect gas behavior. However, for “weakly” imperfect gases, one can prescribe terms that account for Coulomb interactions as corrections to the classic equations. Such corrections are described in reference (23). These corrections can be expressed in the pressure-density-temperature relation using

$$p = \rho R T \sum_{i=1}^N \frac{c_i}{M_i} - p_{\text{correct}} \quad ; \quad p_{\text{correct}} = \frac{K \rho^{3/2}}{\sqrt{T}} \left[ \sum_{i=1}^N \frac{c_i z_i^2}{M_i} \right]^{3/2}, \quad (3)$$

where  $z_i$  is the charge of the  $i$ -th species and the constant  $K = 2.4703 \times 10^{10}$  for  $p$  in N/m<sup>2</sup>. Whereas the energy, density, and mixture properties (mass fractions and molecular weight) are determined from the conservation equations, the temperature,  $T$ , to be used for equation 3 is decoded from the energy using the local density and mixture properties and by iteratively solving

$$e = h(T, c_i) - \frac{RT}{M} - e_{\text{correct}}(\rho, T, c_i) \quad ; \quad e_{\text{correct}} = K \sqrt{\frac{\rho}{T}} \left[ \sum_{i=1}^N \frac{c_i z_i^2}{M_i} \right]^{3/2}, \quad (4)$$

where the enthalpy,  $h$ , is determined using the NASA-Lewis database (24) and the constant  $K = 2.4703 \times 10^7$  for  $e$  in joules per kilogram. It has since been shown (23) that the property determinations obtained from the National Aeronautics and Space Administration (NASA)-Lewis database (24) without modification, such as the enthalpy and specific heats, are reasonably accurate and that the correction terms need not be employed. Thus, use of such corrections will not be continued in this effort. Rather, the mixture temperature and pressure are computed using

$$T = \frac{1}{c_v} \left\{ e - \frac{u^2 + v^2}{2} - \sum_{i=1}^N c_i \Delta H_{f_i}^o \right\}; \quad c_v = \sum_{i=1}^N c_{v_i} c_i + \sum_{i=1}^N h_i \left( \frac{\partial c_i}{\partial T} \right)_v; \quad p = \rho Z R T \sum_{i=1}^N \frac{c_i}{M_i}, \quad (5)$$

where  $Z$  is the compressibility factor for the mixture ( $Z \leq 1$ ). The use of one gas temperature for all species implies thermal equilibrium even though chemical nonequilibrium is utilized in the CFD model.

The species viscosity and thermal conductivity coefficients are given by polynomials with coefficients  $A$ ,  $B$ ,  $C$ , and  $D$  given in reference (24) (coefficients are different for each variable and each species). The mixture values of viscosity and thermal conductivity are computed using the values for each species and empirical mixture rules discussed in reference (20). For each species,  $i$ ,

$$\ln(\mu) = A_{\mu,i} \ln(T) + \frac{B_{\mu,i}}{T} + \frac{C_{\mu,i}}{T^2} + D_{\mu,i} \quad ; \quad \ln(\kappa) = A_{\kappa,i} \ln(T) + \frac{B_{\kappa,i}}{T} + \frac{C_{\kappa,i}}{T^2} + D_{\kappa,i}. \quad (6)$$

A chemical source term appears in equation 1 for each species,  $i$ , denoted,  $w_i$ . Chemical reactions can be expressed in a general reaction rate equation with stoichiometric coefficients for species in these reactions. The chemical source terms that appear in the  $H$  array for equation 1 (i.e.,  $w$ ) are computed using this general reaction rate equation:

$$\frac{dC}{dt} = \frac{w_i}{M_i} = (\nu_i'' - \nu_i') \left( k_f \prod_i^N C_i^{\nu_i'} - k_b \prod_i^N C_i^{\nu_i''} \right), \quad (7)$$

where the  $C$  above represents concentration that is raised to powers of either the ( $\nu$ -prime) or product coefficient ( $\nu$ -double-prime). The forward reaction rate is

$$k_f = C T^n \exp(-E/kT), \quad (8)$$

where the rate data  $C$ ,  $E$ , and  $n$  are given in table 1. The backward rate is computed using the equilibrium constant for each reaction

$$k_b = k_f / K_p \quad ; \quad K_p = \exp \left( -\Delta G / RT \right), \quad (9)$$

where  $K_p$  is the equilibrium constant for a particular reaction computed from the change in Gibbs energy for that reaction (see reference [20] for details). Gibbs energy for each species is computed using the NASA-Lewis tables (see reference [24]).

Where equilibrium chemistry is assumed inside the capillary, resulting in a mixture primarily composed of electrons, C, C<sup>+</sup>, H, and H<sup>+</sup> emerging from the orifice, a chemical kinetics mechanism was developed to describe the finite-rate chemistry that takes place outside the orifice of the capillary as the emerging jet mixes with air (10). An important simplifying

assumption made was that it is sufficient to consider only mixtures which had a concentration of O<sub>2</sub> much greater than that of the plasma constituents; that is, the mixture considered was fuel lean in the combustion sense, the C and H containing species mentioned previously being fuels. We hope to subject this assumption to later scrutiny and, possibly, revision as more complex models are developed in the future. For initial modeling, this assumption was made because fuel-rich chemistry, as might occur in the plasma jet, is known to be extremely complex. The notion that the important mixtures are lean may be reasonable because typical masses of plasma formed during an ETC gun cycle are much smaller than that of the air in the chamber ullage (25).

The chemical mechanism was developed in two stages. First, a detailed mechanism consisting of 224 reactions involving 51 species was compiled. The core of this mechanism was derived from a chemical mechanism developed over the last 10 years for modeling the dark zones of combusting solid propellants (26). To this were added reactions of our choosing that are believed to be the most important involving the charged species and C atoms present in the plasma (these species are not important in propellant dark zones). The addition of reactions beyond those included in the dark zone mechanism were largely guided by thermodynamic considerations and literature review. Most of the rate constants could be obtained from the literature. However, some of the reactions thought to be important have never, to our knowledge, been studied. Rate constants for these had to be estimated. Fortunately, the estimated reactions are all highly exothermic. As a result, it is felt the estimates are likely to be quite good (within a factor of five). Also, because the reactions are expected to be extremely fast, it is unlikely modeling results for gross properties will be very sensitive to the rate coefficients assumed.

The second stage in chemical-mechanism development was reduction of the detailed chemical mechanism to a smaller skeletal mechanism. The skeletal mechanism retains all the elementary reactions found to be important in describing the chemical evolution of a lean plasma/air mixture across a wide range of flowfield temperatures and pressures. This smaller mechanism consists of 57 reactions. Table 1 lists the reactions and rate data (note that the units for C are mole, second, centimeter cubed, and Kelvin,  $E_a/k$  is in units of K; n is nondimensional, whereas k is the Boltzmann constant).

The rate for reaction 5 is of the additive type wherein two rates are computed (for reactions 5 and 5a) and added together for the final rate. The rates for reactions 30, 31, and 55 are of the “falloff” type, wherein the final rate is the product of three factors: two separate rates (e.g., reactions 31 and 31a) and a function based on the local flowfield temperature and mixture,  $F$  ( $T$ , mixture). See reference (10) for further details. The rate data for reactions 5a, 30a, 31a, and 55a are given in table 2. Certain reactions involve a “third-body” or a “collision partner,” which is denoted  $M$ . The species  $M$  can stand for any of the species being considered in the

Table 1. Chemical kinetics mechanism (10).

No.	Reaction	C	n	E/k	Comments
1	H+ + O <sub>2</sub> = H + O <sub>2+</sub>	1.80E + 15	0	0	—
2	C+ + O <sub>2</sub> = CO+ + O	3.00E + 14	0	0	—
3	C+ + O <sub>2</sub> = O+ + CO	3.00E + 14	0	0	—
4	H+ + C = H + C+	1.80E + 15	0	0	—
5	O+ + O <sub>2</sub> = O + O <sub>2+</sub>	8.27E + 14	-0.77	0	See additive rates; 5a
6	O+ + N <sub>2</sub> = NO+ + N	6.00E + 11	0	0	—
7	CO+ + O = O+ + CO	8.40E + 13	0	0	—
8	e + O <sub>2+</sub> = 2O	4.90E + 18	-0.65	0	—
9	e + CO+ = C + O	1.86E + 18	-0.48	0	—
10	e + NO+ = N + O	3.10E + 19	-0.85	0	—
11	C + O <sub>2</sub> = CO + O	5.80E + 13	0	289.88	—
12	O <sub>2</sub> + H = O + OH	3.52E + 16	-0.7	8590.84	—
13	N + NO = N <sub>2</sub> + O	3.27E + 12	0.3	0	—
14	O + NO = N + O <sub>2</sub>	3.80E + 09	1	20822.85	—
15	NO + H = N + OH	1.70E + 14	0	24559.64	—
16	CO + OH = CO <sub>2</sub> + H	1.51E + 07	1.3	-381.48	—
17	H + HO <sub>2</sub> = 2OH	1.69E + 14	0	439.86	—
18	H + HO <sub>2</sub> = H <sub>2</sub> + O <sub>2</sub>	6.63E + 13	0	1069.95	—
19	H + O <sub>2</sub> + M = HO <sub>2</sub> + M	3.61E + 17	-0.72	0	—
20	2OH = O + H <sub>2</sub> O	6.00E + 08	1.3	0	—
21	OH + H <sub>2</sub> = H <sub>2</sub> O + H	2.16E + 08	1.5	1726.22	—
22	H + OH + M = H <sub>2</sub> O + M	1.60E + 22	-2	0	—
23	2H + M = H <sub>2</sub> + M	1.00E + 18	-1	0	—
24	2H + H <sub>2</sub> = 2H <sub>2</sub>	9.20E + 16	-0.6	0	—
25	2H + H <sub>2</sub> O = H <sub>2</sub> + H <sub>2</sub> O	6.00E + 19	-1.25	0	—
26	2H + CO <sub>2</sub> = H <sub>2</sub> + CO <sub>2</sub>	5.49E + 20	-2	0	—
27	OH + HO <sub>2</sub> = H <sub>2</sub> O + O <sub>2</sub>	7.50E + 12	0	0	—
28	NO + HO <sub>2</sub> = NO <sub>2</sub> + OH	2.11E + 12	0	-241.07	—
29	NO <sub>2</sub> + O = NO + O <sub>2</sub>	3.90E + 12	0	-119.78	—
30	NO <sub>2</sub> + M = NO + O	7.60E + 18	-1.27	36884.75	See falloff rates; 30a
31	NO + OH + M = HNO <sub>2</sub> + M	1.99E + 12	-0.05	-362.86	See falloff rates; 31a
32	HNO <sub>2</sub> + OH = H <sub>2</sub> O + NO <sub>2</sub>	1.27E + 10	1	67.94	—
33	CO + NO <sub>2</sub> = NO + CO <sub>2</sub>	9.04E + 13	0	17000.5	—
34	NO <sub>2</sub> + H = NO + OH	1.30E + 14	0	181.68	—
35	HO <sub>2</sub> + CO = CO <sub>2</sub> + OH	5.80E + 13	0	11542.02	—
36	H <sub>2</sub> O <sub>2</sub> + M = 2OH + M	1.30E + 17	0	22898.84	—
37	2HO <sub>2</sub> = H <sub>2</sub> O <sub>2</sub> + O <sub>2</sub>	1.80E + 12	0	0	—
38	H <sub>2</sub> O <sub>2</sub> + OH = H <sub>2</sub> O + HO <sub>2</sub>	1.75E + 12	0	160.04	—
39	O + HO <sub>2</sub> = O <sub>2</sub> + OH	1.40E + 13	0	540.01	—
40	2O + M = O <sub>2</sub> + M	1.89E + 13	0	-899.85	—

Table 1. Chemical kinetics mechanism (10) (continued).

No.	Reaction	C	n	E/k	Comments
41	$\text{NO} + \text{M} = \text{N} + \text{O} + \text{M}$	1.40E + 15	0	74700.55	—
42	$\text{N}_2 + \text{M} = 2\text{N} + \text{M}$	3.71E + 21	-1.6	113236.0 3	—
43	$\text{NH} + \text{M} = \text{N} + \text{H} + \text{M}$	2.65E + 14	0	38002.01	—
44	$\text{NH} + \text{O} = \text{NO} + \text{H}$	5.50E + 13	0	0	—
45	$\text{NH} + \text{O} = \text{N} + \text{OH}$	3.72E + 13	0	0	—
46	$\text{C} + \text{OH} = \text{CO} + \text{H}$	5.00E + 13	0	0	—
47	$\text{O} + \text{H}_2 = \text{OH} + \text{H}$	5.06E + 04	2.67	3165.58	—
48	$\text{CN} + \text{N} = \text{C} + \text{N}_2$	1.04E + 15	-0.5	0	—
49	$\text{CN} + \text{O} = \text{CO} + \text{N}$	2.05E + 13	0	209.86	—
50	$\text{H} + \text{O} + \text{M} = \text{OH} + \text{M}$	6.20E + 16	-0.6	0	—
51	$\text{HO}_2 + \text{O}_3 = \text{OH} + 2\text{O}_2$	8.40E + 09	0	598.89	—
52	$\text{O} + \text{O}_3 = 2\text{O}_2$	4.82E + 12	0	2058.38	—
53	$\text{H} + \text{O}_3 = \text{OH} + \text{O}_2$	8.43E + 13	0	478.11	—
54	$\text{NO} + \text{O}_3 = \text{NO}_2 + \text{O}_2$	1.08E + 12	0	1368.9	—
55	$\text{O} + \text{O}_2 + \text{M} = \text{O}_3 + \text{M}$	3.49E + 12	0	231.5	See falloff rates; 55a
56	$\text{O}^+ + \text{NO} = \text{NO}^+ + \text{O}$	1.00E + 12	0	0	—
57	$\text{O}_2^+ + \text{NO} = \text{O}_2 + \text{NO}^+$	3.00E + 14	0	0	—

Table 2. Rate data for special reactions.

No.	C	n	E/k
5a	5.14E + 13	0	3464.02
30a	2.47E + 28	-3.37	37644.69
31a	5.08E + 23	-2.51	-34.02
55a	8.73E + 16	-1.27	-244.59

mechanism; thus, a single reaction involving  $M$  is actually several reactions with the same reaction rate. Table 3 gives the  $M$  species efficiencies (a value of unity is assumed for species not listed). These factors are multiplied by the concentration of each species in the product-summation terms of equation 6.

Table 3. Reaction rate efficiencies.

Rxn	M	Efficiency	Rxn	M	Efficiency
19	$\text{H}_2\text{O}$	18.6	31	$\text{H}_2\text{O}$	8.3
19	$\text{CO}_2$	4.2	31	$\text{CO}_2$	1.5
19	$\text{H}_2$	2.9	41	$\text{H}_2$	2.2
19	CO	2.1	41	$\text{H}_2\text{O}$	6.7
19	$\text{N}_2$	1.3	41	$\text{CO}_2$	3
22	$\text{H}_2\text{O}$	5	41	$\text{H}_2\text{O}$	5
23	$\text{H}_2$	0	50	$\text{N}_2$	1.48
23	$\text{CO}_2$	0	55	$\text{O}_2$	1.61
23	$\text{CO}_2$	0	55	CO	1.76
30	$\text{H}_2\text{O}$	4.4	55	$\text{CO}_2$	4.17
30	$\text{CO}_2$	2.3	55	$\text{H}_2\text{O}$	15

---

## 5. Results and Discussion

---

The computational domain chosen to simulate the Penn State University experiment (figure 3) is shown in figure 6 and is similar to that used to simulate the ARL experiment sketched in figure 2. In each case, this domain extends from the capillary/extender-tube on the left to the plate on the right (19 mm) and from the centerline of the capillary (and plate) to a fixed radial distance (40 mm) that is determined by the distance from the plate centerline to the pressure probe designated P1 and includes a small radial distance beyond. This region was discretized using 154 axial grid cells and 295 radial grid cells, distributed with essentially even spacing throughout as shown in figure 6. Some degree of radial grid clustering was used up to 0.015 m in order to more accurately resolve the formation of important gas dynamic phenomena (expansions, shocks and turbulent mixing). The boundary conditions for the region are symmetry on the axis ( $Y = 0$ ), outflow at  $Y = 0.04$  m, no-slip/no-penetration on the capillary housing surface ( $X = 0, 0.0015 < Y < 0.04$  m) and on the plate surface, specified inflow at the capillary exit ( $X = 0, 0 < Y < 0.015$  m). Initially, the entire flowfield is filled with air (0.8 mole fraction of  $N_2$  and 0.2 mole fraction of  $O_2$ ). Figure 7 shows the current amplitude variation for a typical experiment. Given the amplitude/time and the physical characteristics of the capillary, the capillary model (11) generates the range of density, velocity, pressure, temperature, and species distributions shown in figures 8–10. The inflow conditions for the computational domain follow from those displayed in these figures. Figure 10 shows that there are five prominent species in the plasma efflux from the 29 species that were considered in the capillary model (11). The CFD simulation includes 39 species (10 species added for reaction with air): electrons, C,  $C^+$ ,  $C^{++}$ ,  $C^-$ , CH,  $CH^+$ , CN,  $CN^+$ , CO,  $CO^+$ ,  $C_2$ ,  $C_2^+$ , H,  $H^+$ ,  $H^-$ ,  $H_2$ ,  $H_2^+$ , N,  $N^+$ , NH,  $NH^+$ , NO,  $NO^+$ ,  $N_2$ ,  $N_2^+$ , O,  $O^+$ , OH,  $OH^+$ ,  $O_2$ ,  $O_2^+$ ,  $H_2O$ ,  $H_2O_2$ ,  $HNO_2$ ,  $NO_2$ ,  $CO_2$ , and  $O_3$ .

To aid in the interpretation of computational results for the plasma jet, figure 11 shows a schematic of the gas dynamic features expected in highly underexpanded supersonic jets (27, 28). The efflux of plasma from the inlet generates a weak precursor shock (A) that expands spherically. Behind this shock is air; the plasma is entirely contained by this shock and is separated from the air by an irregularly shaped contact surface (B) across which pressure and velocity are preserved, but entropy changes discontinuously. Expansion waves (Mach cone) generate at the inlet (C), travel to the precursor shock (A), are reflected as weak compression waves, and coalesce into a strong oblique shock, or barrel shock, (D), within the plasma jet. This barrel shock (D) terminates in an irregular reflection that forms a triple-point (E) joining the barrel shock (D), its reflection (F), and a normal shock (G) or Mach disk. Whereas, the precursor shock (A) is relatively weak and diffuse, producing a mildly supersonic flow, the barrel shock (D) and Mach disk (G) are strong shocks that enclose a fully supersonic flow region.

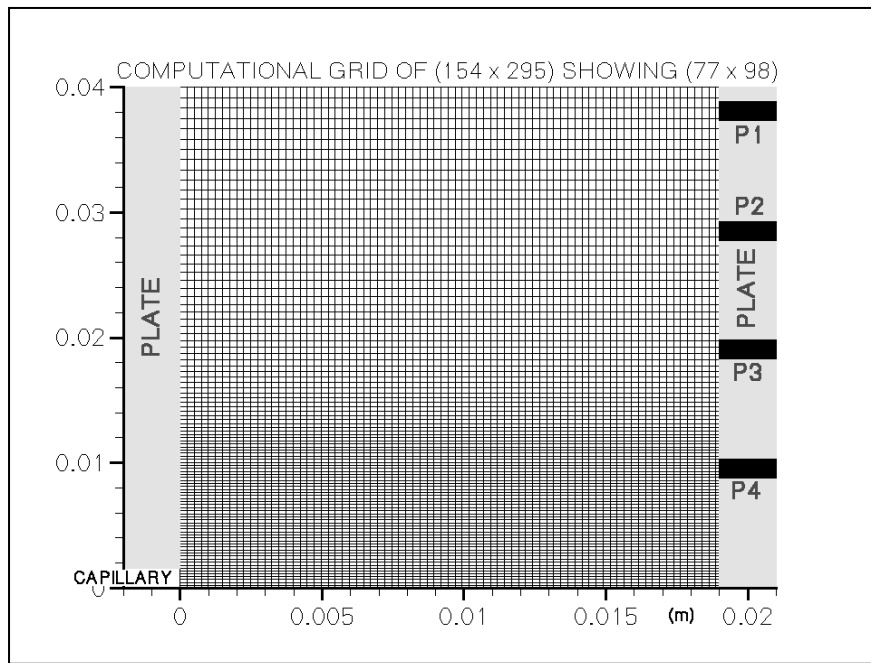


Figure 6. Computational grid used for the simulation of the Penn State University open-air plate experiment. Lower boundary corresponds to the capillary and plate centerline. Partial grid shown for clarity.

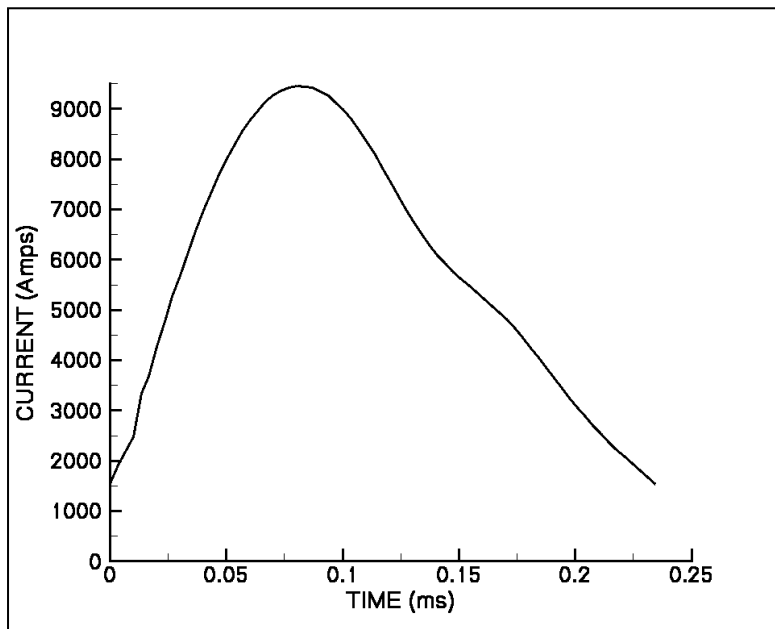


Figure 7. Current history.

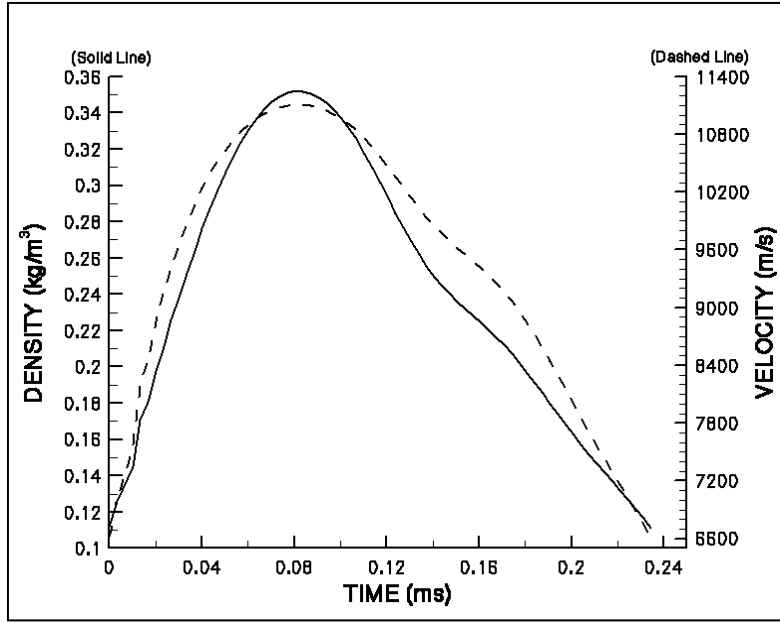


Figure 8. Efflux density and velocity histories.

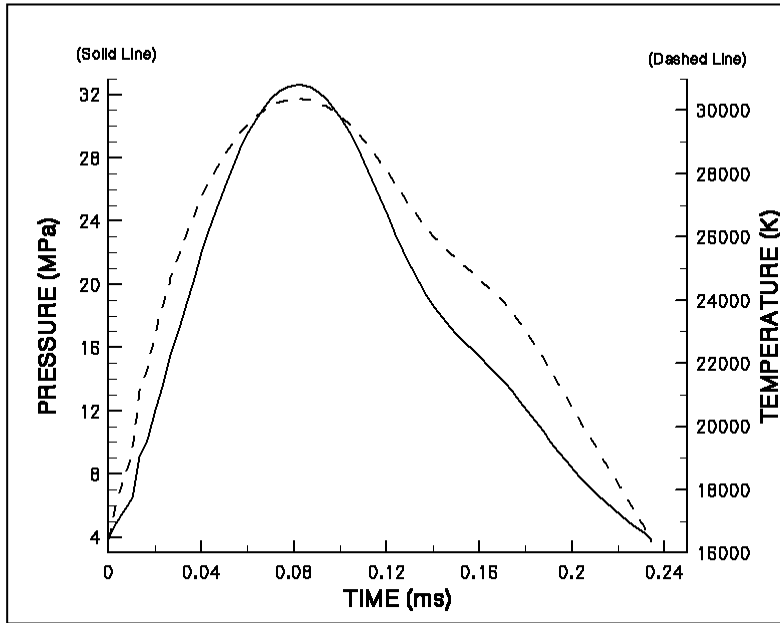


Figure 9. Efflux pressure and temperature histories.

Figures 12–18 show the time history of the plasma jet from shortly after entrance into open-air (0.0208 ms) to long after impact upon the plate and near the final stages of efflux from the capillary (0.241 ms). Note that the frames in figures 12–18 are not plotted to scale. Mach number contours are displayed in gray-scale from 0 (bright white) to 1.5 and above (dark black). Temperature contours are displayed in gray-scale from 300 K and below (bright white) to 28,000 K and above (dark black).

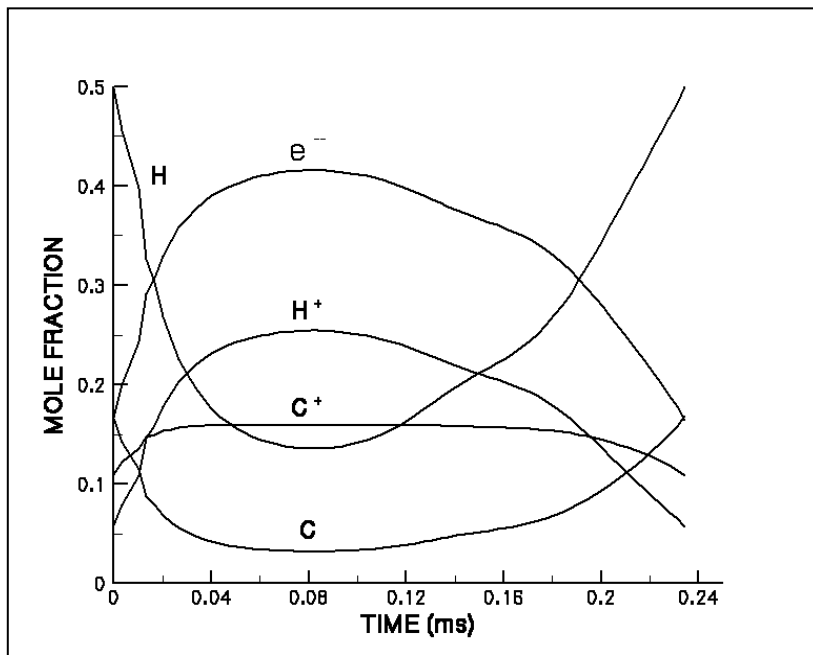


Figure 10. Efflux species mole fraction histories.

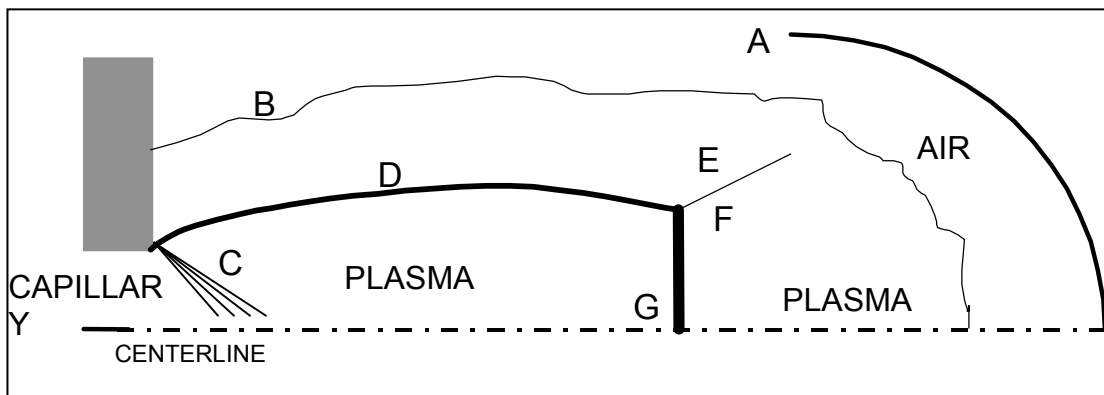


Figure 11. Schematic of gasdynamic features in a highly underexpanded jet.

The low-density and high-pressure plasma efflux enters the open-air as a highly underexpanded jet. An expansion wave forms at the capillary exit. A precursor shock is also formed as the jet is moving at  $\sim 6800$  m/s at this time, or  $\sim$ Mach 1.7, based on the local sound speed in the mixture (note that the plasma gas is of very low molecular weight,  $\sim 4.3$  g/mole). By  $\sim 0.0458$  ms (figure 13), the predominant gas dynamic features in the jet have been established, including the barrel shocks (seen better in temperature contours), the intersection of the barrel shock with the Mach disk ( $X = 0.011$  m,  $Y = 0.006$  m, figure 13a), and a weak reflected shock (seen more clearly in figure 14a). Due to the variable viscosity in the flowfield (see equation [5]), the precursor shock is more diffuse than the normal shock of the Mach disk or the oblique barrel

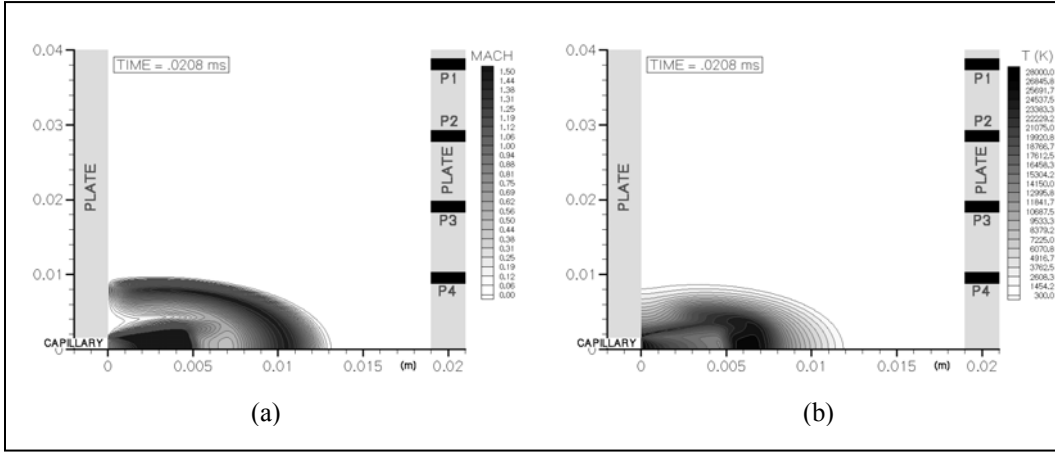


Figure 12. Computed (a) Mach number contours and (b) temperature contours at time = 0.0208 ms.

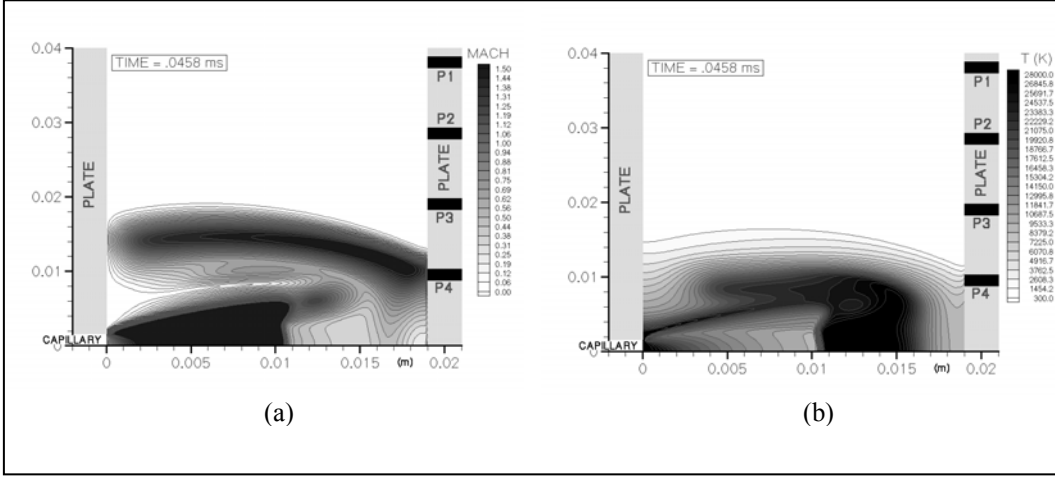


Figure 13. Computed (a) Mach number contours and (b) temperature contours at time = 0.0458 ms.

shock (note the subsonic flow region between the normal shock and the precursor shock [light gray region in Mach number and dark region in temperature of figure 13]; within this region resides the contact surface). The precursor shock reaches the plate at  $\sim 0.0458$  ms. Stagnation of supersonic flow on the plate causes a shock reflection that moves back toward the capillary as the precursor shock travels along the plate (figures 13 and 14). This causes the Mach disk to recede slightly and then settle at a position 0.01 m from the capillary (figure 14a). At this stage, a layer of high-pressure and high-temperature gas is held on the plate near the centerline (i.e., plate stagnation region). The plasma efflux is near peak output (recall figures 7–10).

Figures 15–18 show the computed results for times when the plasma efflux is waning; by 0.241 ms, the plasma jet has ceased (figure 18). At 0.1192 ms, the Mach disk is greatly reduced in size as the barrel shock dips toward the centerline and the reflected shock (at the

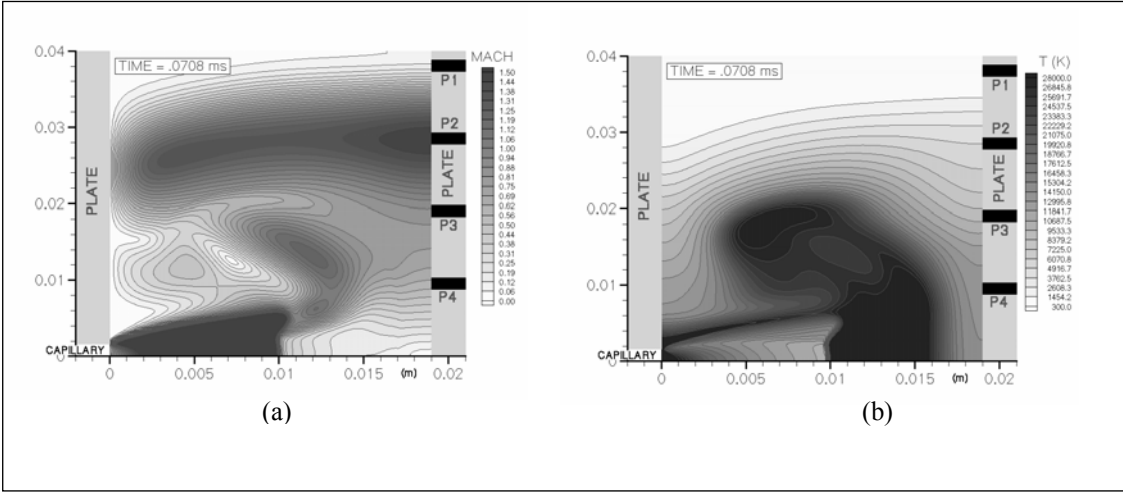


Figure 14. Computed (a) Mach number contours and (b) temperature contours at time = 0.0708 ms.

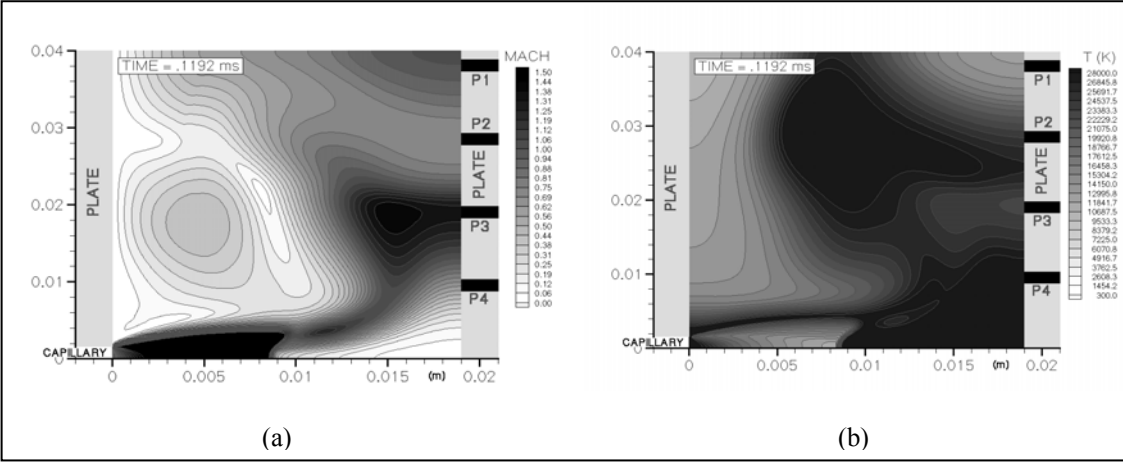


Figure 15. Computed (a) Mach number contours and (b) temperature contours at time = 0.1192 ms.

intersection of the Mach disk and the barrel shock) impacts the plate near the pressure-tap P3 (figure 15a). Multiple shock reflections from the plate are seen to subsequently occur (figure 17a), resulting in a shroud or layer of high-pressure, high-temperature gas along the plate surface. As the plasma efflux ceases (figure 18), the plate slowly begins to return to ambient conditions. Figure 19 displays these events as time-history plots of pressure at each of the pressure-tap locations (P1–P4). An additional tap location, P0, was added on the centerline of the plate, but has no experimental equivalent. The precursor shock is seen to arrive at the plate (figure 19, tap P0) at ~0.04 ms and subsequently traverses each of the tap locations in sequence. In each case, the pressure is momentarily raised to 10's or 100's of MPa and then rapidly relaxes to much smaller values. As further flow dynamics proceed, as previously described, the tap locations re again pressurized and relaxed. Eventually, pressure levels at all tap locations

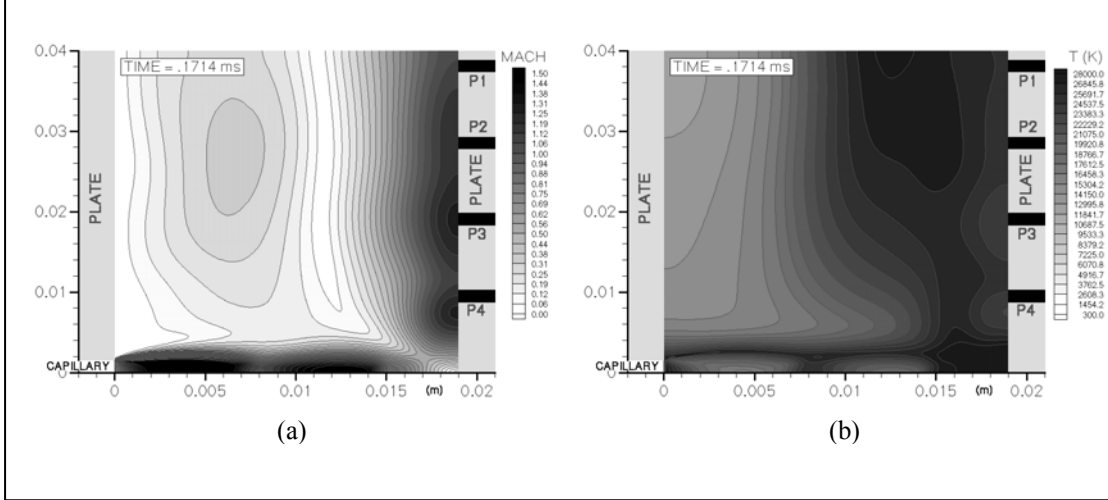


Figure 16. Computed (a) Mach number contours and (b) temperature contours at time = 0.1494 ms.

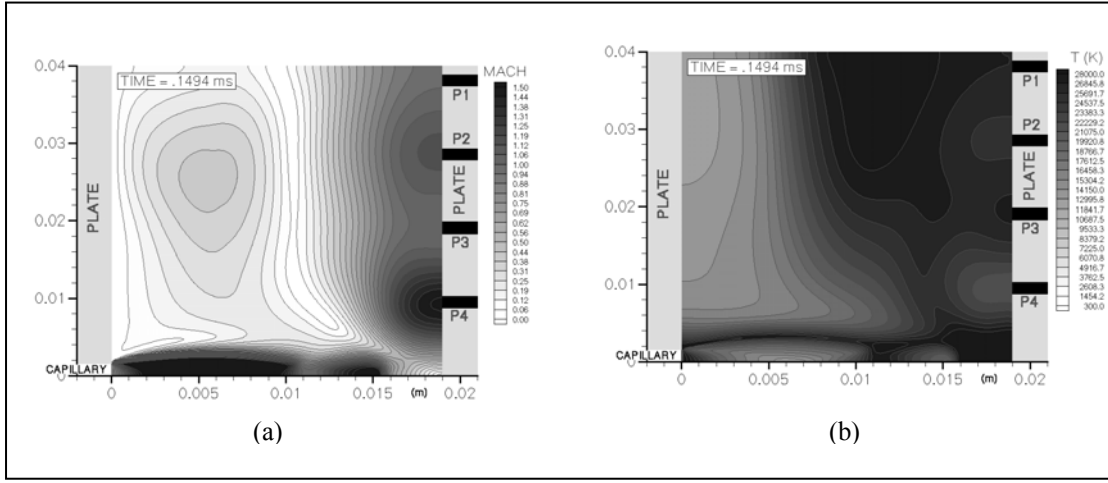


Figure 17. Computed (a) Mach number contours and (b) temperature contours at time = 0.1714 ms.

relax to the ambient value (not shown in the figure). This highly transient flow has important consequences for tests of the ignition and sustained combustion of a solid propellant sample to be held on the plate.

Figures 20 and 21 show comparisons between the computed and measured pressures. Figure 20 displays the computed and measured pressure peaks (maximums) and the corresponding time-of-arrival of the precursor shock. The results for a 19-mm standoff of the plate compare well with the measured values. In general, the computed shock velocity is too high, perhaps due to the absence of capillary residue (i.e., particles from the vaporization of the polyethylene liner) in the simulation. The translation of these particles would remove energy from the flow and reduce the mean velocity. This would explain the overprediction of peak pressures at the P4

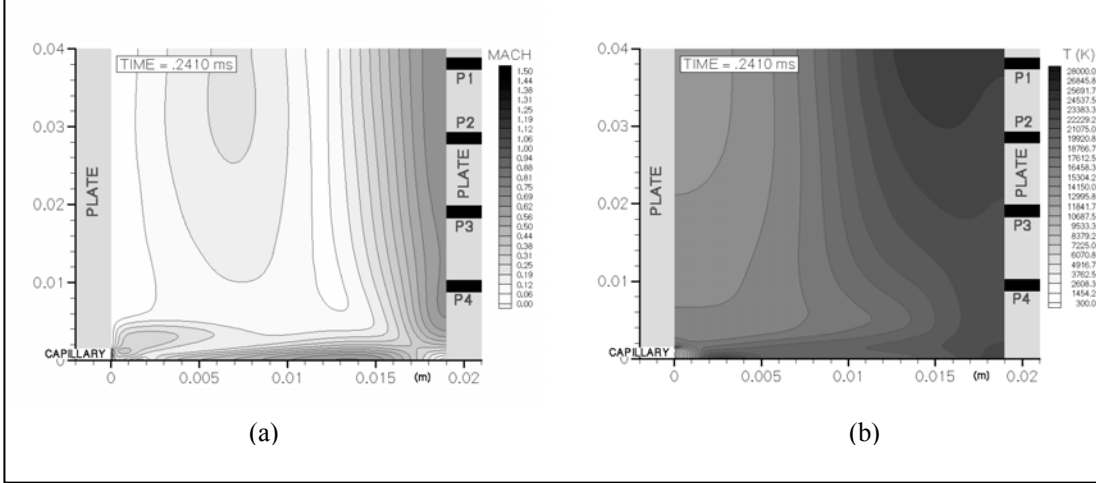


Figure 18. Computed (a) Mach number contours and (b) temperature contours at time = 0.2410 ms.

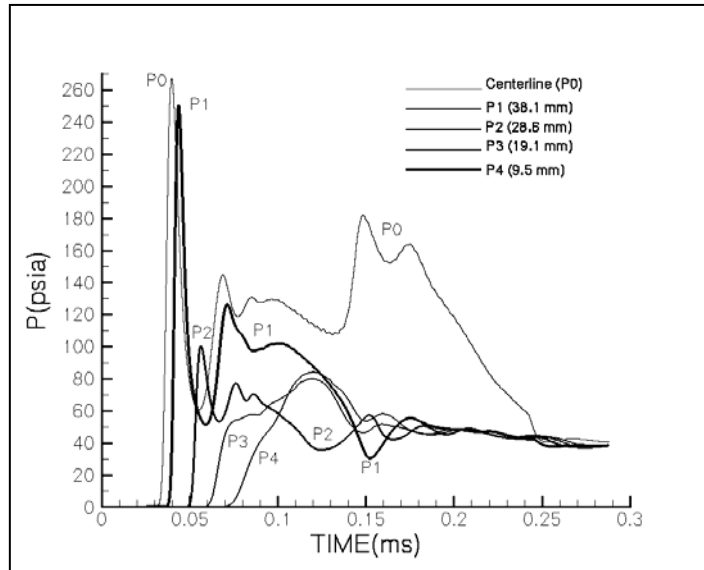


Figure 19. Computed pressures at plate taps.

tap location, where most of the particles are usually found to accumulate (14). Figure 21 compares the P4 and the P1 tap locations. Predicted results for the P4 tap location have been shifted in time by 0.022 ms in order to line up the arrival time for the precursor shock. With this adjustment, the timing of subsequent pressure peaks are well predicted by the code, but the pressure levels are too low. It is interesting to note that the pressure decrease at a time of 0.17 ms (figure 21a) is predicted. This pressure drop corresponds to a flow expansion near the P4 tap location at this time (see figure 17a). The results for the P1 tap location are also encouraging (no adjustments have been made) because the pressure peaks occur at regular time intervals for both the predicted and measured data; however, the predicted pressures are too high.

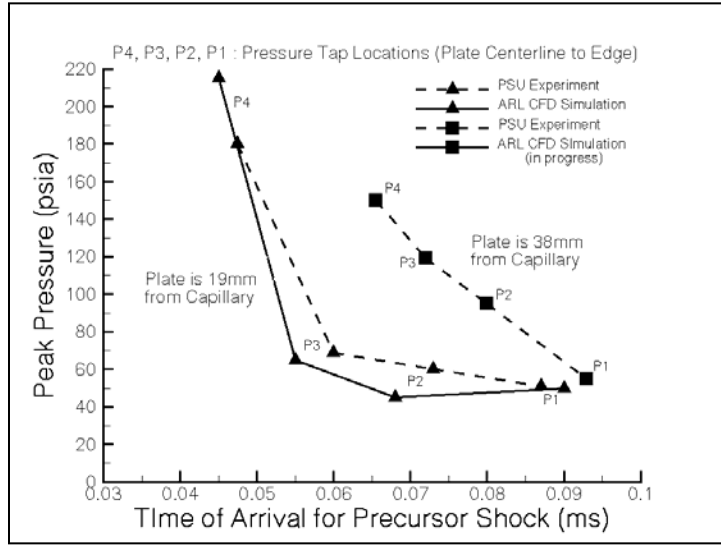


Figure 20. Peak pressure data and computations.

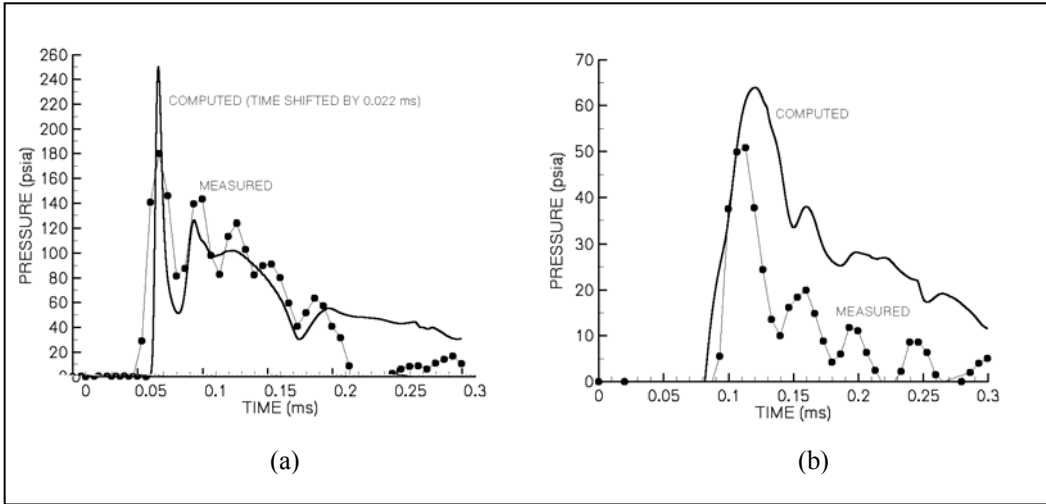


Figure 21. Computed and measured pressure histories at (a) P4 and (b) P1 tap locations.

The results of figures 20 and 21 demonstrate that the CFD code is able to track the dynamics of the flowfield even if the computed pressure levels are often too high. Again, the absence of particles in the simulation as well as the uncertainties in thermodynamic and transport relations for an ionized gas at these temperatures may explain some of the discrepancies.

Figures 22–24 display some of the chemical aspects of the flowfield. Figure 22 shows the time histories of the major species at the plate centerline (i.e., referred to the P0 tap location) and at the tap location farthest from the plate centerline (i.e., P1). Comparison of these figures with

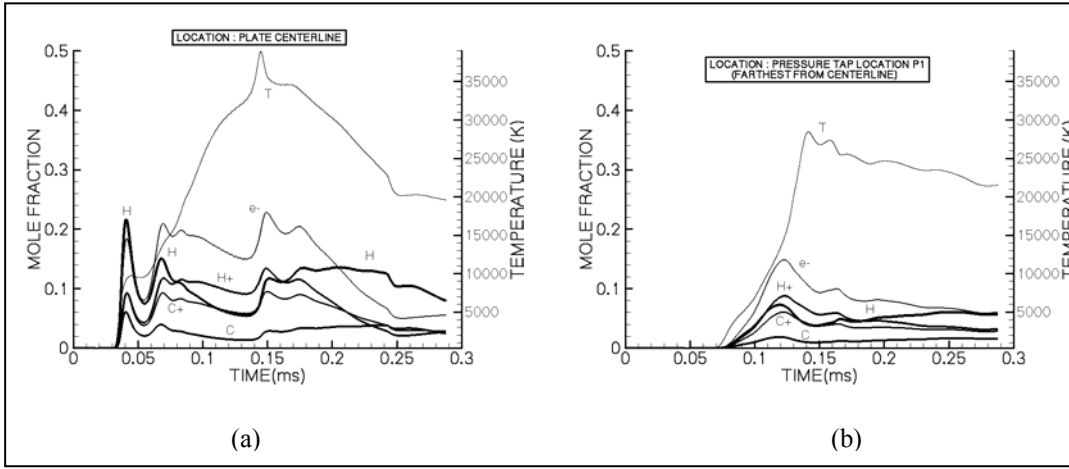


Figure 22. Computed time variation of mole fractions at two locations on the plate.

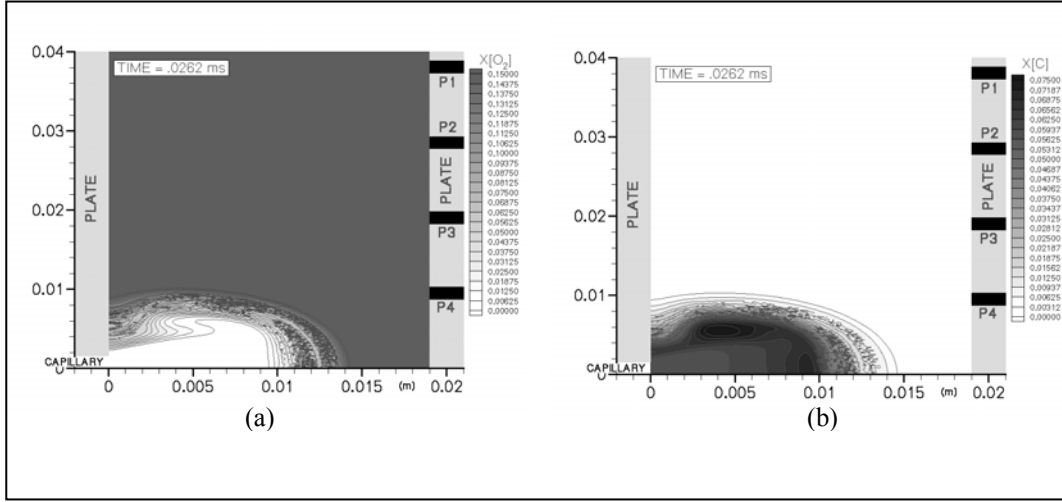


Figure 23. Computed mole fraction contours for (a)  $O_2$  and (b)  $C$  at time = 0.0262 ms.

figure 10 (the species distributions at the capillary exit) shows that a large proportion of the ion species are actually deposited onto the plate which are expected to ultimately affect the ignition and combustion characteristics of propellant mounted on the plate. Figure 23 and figure 24a are gray scale mole fraction contours of diatomic oxygen, atomic carbon, and carbon monoxide.

These results show that while the plasma is devoid of  $O_2$  (large white region extending to 0.01 m in figure 23a), there is some  $O_2$  in a mixing layer on the edge of the plasma efflux (note region between 0.01 and 0.014 m) as well as atomic carbon that has diffused outward from the plasma jet. These combine chemically to form CO (figure 24a) in this mixing region, albeit at very low levels ( $1.0 \times 10^{-10}$ ). After impact with the plate, CO is continually formed in the stagnation region of the plate (figure 24b). It can be concluded that some mixing between the plasma

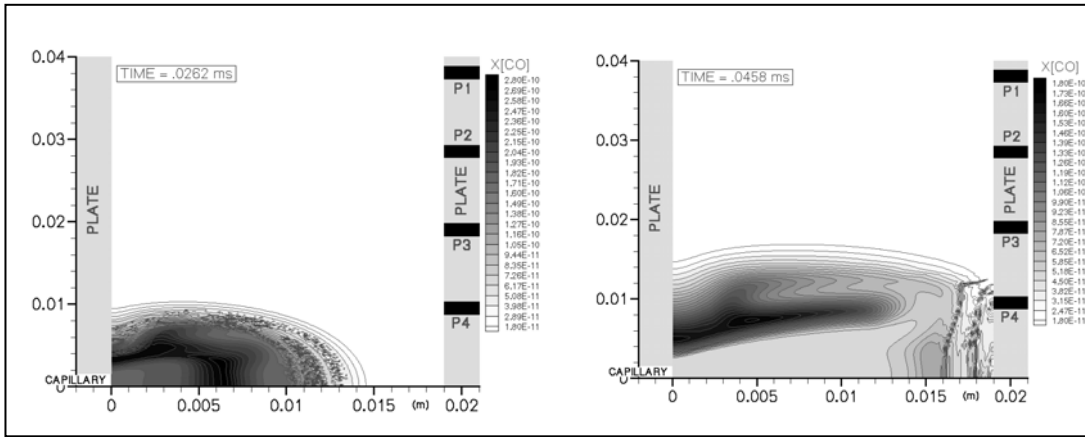


Figure 24. Computed mole fraction contours for CO at times = (a) 0.0262 and (b) 0.0458 ms.

species and the air does occur and that this mixing promotes a low level of chemical reaction. Of course, these results are dependent on the plasma/air chemical mechanism employed in this study and therefore warrant further study.

## 6. Conclusions

A time-accurate CFD code has been applied to the modeling of the high-temperature chemically reactive plasma efflux from an ETC igniter fired into open air and impinging on an instrumented plate. The CFD code has been linked to a plasma capillary model for purposes of specification of the exit conditions of the igniter. The major features of this efflux have been resolved by numerical simulation revealing a highly underexpanded jet with a strong precursor shock, a

barrel shock that reflects at a triple-point, and a normal shock or Mach disk. Impact of the jet upon a plate generates a stagnation region, a reflected shock that travels back toward the capillary, and a normal shock that traverses the plate. As the plasma efflux wanes, the barrel shock reflects from the centerline and then the plate, causing a subsequent series of pressure waves along the plate. Evidence of this shock system and pressure wave system is seen in both the experimental data and the prediction. The presence of this shock system has important implications for mechanical damage to solid propellant exposed to the plasma efflux. Chemical conditions at the plate are quite different from those at the ETC igniter. The model indicates that ions are present at the plate and that mixing (and reaction) between the plasma species and the air is present in a narrow region near the efflux jet. These computer simulations represent a unique, detailed modeling of ETC igniter plasma efflux.

---

## 7. References

---

1. Del Güercio, M. A. Propellant Burn Rate Modification by Plasma Injection. *Proceedings of the 34th JANNAF Combustion Subcommittee Meeting*, West Palm Beach, FL, October 1997; CPIA Publication 662, Vol. 1, pp 35–42.
2. Perelmutter, L.; Sudai, M.; Goldenberg, C.; Kimhe, D.; Zeevi, Z.; Arie, S.; Melnik, M.; Melnik, D. Temperature Compensation by Controlled Ignition Power in SPETC Guns. *Proceedings of the 16th International Symposium on Ballistics*, San Francisco, CA, September 1996; NDIA, Vol. 1, pp 145–152.
3. Dyvik, J. A.; Katulka, G. ETC Temperature Compensation; Experimental Results of 120-mm Test Firings. *Proceedings of the 33rd JANNAF Combustion Subcommittee Meeting*, Monterey, CA, November 1996; CPIA Publication 653, Vol. 3, pp 111–119.
4. Katulka, G. L.; Dyvik, J. A. Experimental Results of Electrical Plasma Ignition in 120-mm Solid Propellant Tank Gun Firings. *Proceedings of the 33rd JANNAF Combustion Subcommittee Meeting*, Monterey, CA, November 1996; CPIA Publication 653, Vol. 3, pp 103–110.
5. White, K. J.; Katulka, G. L.; Khuan, T.; Nekula, K. *Plasma Characterization for Electrothermal-Chemical (ETC) Gun Applications*; ARL-TR-1491; U.S. Army Research Laboratory: Aberdeen Proving Ground, MD, 1997.
6. Perelmutter, L.; Goldenberg, C.; Sudai, M.; Alimi, R.; Furman, M.; Kimhe, D.; Appelbaum, G.; Arie, S.; Zeevi, Z.; Melnik, D. Experimental Study of Plasma Propagation and Ignition of Solid Propellant in a Gun Chamber. *Proceedings of the 16th International Symposium on Ballistics*, San Francisco, CA, September 1996.
7. Nusca, M. J.; White, K. J. Plasma Radiative and Convective Interactions With Propellant Beds. *Proceedings of the 34th JANNAF Combustion Subcommittee Meeting*, West Palm Beach, FL, October 1997; CPIA Publication 662, Vol. 1, pp 21–42.
8. White, K. J.; Williams, A. W.; Nusca, M. J. Plasma Output and Propellant Radiation Absorption Characteristics. *Proceedings of the 35th JANNAF Combustion Subcommittee Meeting*, Tucson, AZ, December 1998; CPIA Publication 680, Vol. 1, pp 237–246.
9. Kaste, P. J.; Birk, A.; Del Güercio, M. A.; Lieb, R.; Kinkennon, A. Surface Phenomena of Plasma-Treated Propellant Samples. *Proceedings of the 36th JANNAF Combustion Subcommittee Meeting*, Cocoa Beach, FL, October 1999; CPIA Publication 691, Vol. 2, pp 77–98.

10. Anderson, W. R.; Schroeder, M. A. Chemical Mechanism for ETC Plasma Interaction With Air. *Proceedings of the 36th JANNAF Combustion Subcommittee Meeting*, Cocoa Beach, FL, October 1999; CPIA Publication 691, Vol. 2, pp 43–54.
11. McQuaid, M. J.; Nusca, M. J. *Calculating the Chemical Compositions of Plasmas Generated by an Ablating-Capillary Arc Ignition System*; ARL-TR-2046; U.S. Army Research Laboratory: Aberdeen Proving Ground, MD, 1999.
12. Williams, A. W.; White, K. J. Plasma-Propellant Interaction Studies: Measurements of In-Depth Propellant Heating by Plasma Radiation; Investigation of Possible Plasma-Induced Propellant Erosion. *Proceedings of the 36th JANNAF Combustion Subcommittee Meeting*, Cocoa Beach, FL, October 1999; CPIA Publication 691, Vol. 2, pp 67–76.
13. Beyer, R. A. Small Scale Experiments in Plasma Propellant Interactions. *Proceedings of the 37th JANNAF Combustion Subcommittee Meeting*, Monterey, CA, November 2000; CPIA Publication 701, Vol. 1, pp 137–144.
14. Litzinger, T. A.; Li, J.-Q.; Zhou, H.; Kudva, G.; Thynell, S. Plasma Propellant Interactions: Experiments and Modeling. *Proceedings of the 37th JANNAF Combustion Subcommittee Meeting*, Monterey, CA, November 2000; CPIA Publication 701, Vol. 1, pp 109–121.
15. Nusca, M. J.; White, K. J.; Landsberg, A. M.; Lind, C. A.; Young, T. R. Computational Simulations of ETC Igniters and Plasma Discharge Experiments. *Proceedings of the 35th JANNAF Combustion Subcommittee Meeting*, Tucson, AZ, December 1998; CPIA Publication 680, Vol. 1, pp 219–227.
16. Nusca, M. J.; White, K. J.; Williams, A. W.; Landsberg, A. M.; Young, T. R.; Lind, C. A. Computational and Experimental Investigations of Open-Air Plasma Discharges. *The 37th American Institute of Aeronautics and Astronautics, Aerospace Sciences Meeting*, Reno, NV, January 1999; AIAA Paper 99-0865.
17. Boris, J. P.; Landsberg, A. M.; Oran, E. S.; Gardner, H. *LCPFCT—A Flux-Corrected Transport Algorithm for Solving Generalized Continuity Equations*; NRL-MR-93-7192; U.S. Naval Research Laboratory: Washington, DC, 1993.
18. Powell, J.; Zielinski, A. *Theory and Experiment for an Ablating-Capillary Discharge and Application to Electrothermal Chemical Guns*; BRL-TR-3355; U.S. Army Ballistic Research Laboratory: Aberdeen Proving Ground, MD, 1992.
19. Nusca, M. J.; McQuaid, M. J.; Anderson, W. A. Numerical Simulation of an Open-Air Plasma Jet Using a Multi-Species Reacting Flow CFD Code. *Proceedings of the 25th American Institute of Aeronautics and Astronautics, Plasmadynamics and Lasers Conference*, Denver, CO, June 2000.

20. Nusca, M. J. Numerical Simulation of Electromagnetic Wave Attenuation in Nonequilibrium Chemically Reacting Flows. *Computers and Fluids* **1998**, 27 (2), 217–238.
21. Nusca, M. J. Numerical Simulation of the Ram Accelerator Using a New Chemical Kinetics Mechanism. *Journal of Propulsion and Power* **2002**, 18 (1), 44–52.
22. Nusca, M. J.; Dinavahi, S. P. G.; Soni, B. Grid Adaptation Studies for Reactive Flow Modeling of Propulsion Systems. *37th American Institute of Aeronautics and Astronautics Aerospace Sciences Meeting*, Reno, NV, January 1999; AIAA Paper 99-0970.
23. McQuaid, M. J.; Nusca, M. J. *Thermodynamic Property Characterization of Plasmas Generated by an Ablating-Capillary Arc*; ARL-TR-2427; U.S. Army Research Laboratory: Aberdeen Proving Ground, MD, 2001.
24. McBride, B. J.; Gordon, S. *Computer Program for Calculation of Complex Chemical Equilibrium Compositions and Applications, II. Users Manual and Program Description*; NASA RP 1311; Washington, DC, June 1996.
25. Alimi, R.; Goldenberg, C.; Perelmutter, L.; Melnik, D.; Zoler, D. A Solid-Phase Model for Plasma Ignition of Solid Propellant. *Proceedings of the 4th International Symposium on Special Topics in Chemical Propulsion*, Stockholm, Sweden, May 1999.
26. Anderson, W. R.; Ilincic, N.; Meagher, N. E.; Seshadri, K.; Vanderhoff, J. A. Detailed and Reduced Chemical Mechanisms for the Dark Zones of Double Base and Nitramine Propellants in the Intermediate Temperature Regime. *32nd JANNAF Combustion Subcommittee Meeting and 1995 Propulsion Systems Hazards Subcommittee Meeting, Joint Sessions*; Chemical Propulsion Information Agency, Publication 638, Vol. 1, p 197.
27. Wilson, D. E.; Raja, L. L.; Petviashvili, N. Theoretical Analysis of the External Pulsed Propellant and Plasma Jets. *36th American Institute of Aeronautics and Astronautics, Aerospace Sciences Meeting*, Reno, NV, January 1998; AIAA Paper 98-1000.
28. Schmidt, E. M.; Shear, D. D. Optical Measurements of Muzzle Blast. *American Institute of Aeronautics and Astronautics* **1975**, 13 (8), 1086–1091.

<u>NO. OF COPIES</u>	<u>ORGANIZATION</u>	<u>NO. OF COPIES</u>	<u>ORGANIZATION</u>
1 (PDF Only)	DEFENSE TECHNICAL INFORMATION CTR DTIC OCA 8725 JOHN J KINGMAN RD STE 0944 FT BELVOIR VA 22060-6218	1	<u>ABERDEEN PROVING GROUND</u> DIR USARL AMSRD ARL CI OK TP (BLDG 4600)
1	COMMANDING GENERAL US ARMY MATERIEL CMD AMCRDA TF 5001 EISENHOWER AVE ALEXANDRIA VA 22333-0001		
1	INST FOR ADVNCD TCHNLGY THE UNIV OF TEXAS AT AUSTIN 3925 W BRAKER LN STE 400 AUSTIN TX 78759-5316		
1	US MILITARY ACADEMY MATH SCI CTR EXCELLENCE MADN MATH THAYER HALL WEST POINT NY 10996-1786		
1	DIRECTOR US ARMY RESEARCH LAB AMSRD ARL CS IS R 2800 POWDER MILL RD ADELPHI MD 20783-1197		
3	DIRECTOR US ARMY RESEARCH LAB AMSRD ARL CI OK TL 2800 POWDER MILL RD ADELPHI MD 20783-1197		
3	DIRECTOR US ARMY RESEARCH LAB AMSRD ARL CS IS T 2800 POWDER MILL RD ADELPHI MD 20783-1197		

NO. OF  
COPIES ORGANIZATION

ABERDEEN PROVING GROUND

31 DIR USARL  
AMSRD ARL WM BD  
W ANDERSON  
R BEYER  
A BRANT  
S BUNTE  
L CHANG  
T COFFEE  
J COLBURN  
P CONROY  
G COOPER  
B FORCH  
A HORST  
S HOWARD  
S KARNA  
P KASTE  
A KOTLAR  
M MCQUAID  
A MIZIOLEK  
J NEWILL  
M NUSCA (6 CPS)  
R PESCE-RODRIQUEZ  
P PLOSTINS  
B RICE  
J SAHU  
S SILTON  
P WEINACHT  
A WILLIAMS

INTENTIONALLY LEFT BLANK.